PHYSICAL REVIEW APPLIED **19,** 034004 (2023)

Structural-Stability Study of Antiperovskite Na_3OCl for Na-Rich Solid Electrolyte

Tan-Lien Pham,[1,‡] Woon Ih Choi,[2,*,‡] Aamir Shafique,[1] Hye Jung Kim,[3] Munbo Shim,[2]
Kyoungmin Min,[4] Won-Joon Son,[2] Inkook Jang,[2] Dae Sin Kim,[2] Mauro Boero,[5] Carlo Massobrio,[5]
Guido Ori,[5] Hyo Sug Lee,[6] and Young-Han Shin[1,†]

[1] *Department of Physics, Multiscale Materials Modeling Laboratory, University of Ulsan, Ulsan 44610, Republic of Korea*
[2] *Computational Science and Engineering (CSE) Team, Innovation Center, Samsung Electronics, Hwaseong-si 18448, Republic of Korea*
[3] *Department of Physics, Pusan National University, Busan 46241, Republic of Korea*
[4] *School of Mechanical Engineering, Soongsil University, 369 Sangdo-ro, Dongjak-gu, Seoul 06978, Republic of Korea*
[5] *Université de Strasbourg, CNRS, Institut de Physique et Chimie des Matériaux de Strasbourg, UMR 7504, Strasbourg F-67034, France*
[6] *Samsung Advanced Institute of Technology, Suwon 16678, Republic of Korea*

(Received 20 July 2022; revised 30 November 2022; accepted 20 December 2022; published 1 March 2023)

The structural phase transition of the high-symmetry cubic phase of antiperovskite Na_3OCl is investigated by computing the phonon band structures of 14 different polymorphs with distinct types of ONa_6 octahedral tilting. The resulting P-T phase diagram shows that, at high temperature and low pressure, the high-symmetry cubic structure with $Pm\bar{3}m$ symmetry is the most stable phase. At low temperature and high pressure, on the other hand, the monoclinic structure with $P2_1/m$ symmetry becomes the most stable phase. In between those two, there is a region in the phase diagram where the orthorhombic structure with *Bmmb* symmetry is the most stable phase. To improve upon the quasiharmonic results, we do additional calculations in the framework of the self-consistent phonon (SCP) theory, including lattice anharmonicity by using cubic and quartic interatomic force constants (IFCs). This is particularly important for the high-symmetry cubic phase. We find that by decreasing the temperature, the frequency of the soft phonon at the M and R symmetry points gradually shifts to lower values. From these results, we can infer that a phase transition occurs around 166–195 K upon soft-mode condensation. Due to the proximity of the soft-mode frequencies at both symmetry points R and M, we expect a cubic-to-orthorhombic phase transition to be realized via simultaneous condensation of the two octahedral tilting modes.

DOI: 10.1103/PhysRevApplied.19.034004

I. INTRODUCTION

While Li-ion batteries have been widely used in portable electronic devices and electric vehicles due to their high performance, their prospects in large-scale grid-level storage of renewables are severely restricted by the limited availability of Li [1–3]. Because of the higher abundance of Na compared to Li [4,5], Na-ion batteries have recently been gaining attention [6,7]. In addition, to minimize the hazards such as leakage of corrosive, toxic, and flammable organic liquid electrolytes, solid electrolytes have been suggested as alternatives to conventional liquid electrolytes [8–10] and studies of solid electrolytes such as alkali-metal oxyhalides have attracted considerable attention [1,7,11–13].

In our previous work, we have performed first-principles calculations for 14 different octahedrally tilted Na_3OCl structures and found that they are energetically more stable than the high-symmetry cubic phase by 11–16 meV per stoichiometric unit. Phonon spectra, computed within the harmonic approximation, have shown that the monoclinic phase with $P2_1/m$ symmetry and the orthorhombic phase with *Pnma* symmetry have no imaginary modes, thus providing a fingerprint of the stability of these systems. Yet, the absence of imaginary frequencies is not always a sufficient criterion by which to assess the stability of a system. Depending on the environmental conditions, the presence

---

[*] wooni.choi@samsung.com
[†] hoponpop@ulsan.ac.kr
[‡] These two authors contributed equally.

of imaginary modes can still correspond to stable systems. For example, well-known perovskite oxides such as $SrTiO_3$, $BaTiO_3$, and $PbTiO_3$ do have imaginary frequencies in the harmonic phonon band structure of its cubic phases that are stabilized above certain temperatures [14–16]. Likewise, to better understand the phase-transition characteristics of Na_3OCl, which has the same symmetry, we need to consider the Gibbs free energy of its possible structures with respect to environmental parameters such as pressure and temperature [17].

Until recently, information on the enthalpies of formation for Na_3OCl and its thermodynamic properties and phase change have not been available. Despite the experimental synthesis and identification of the cubic $Pm\bar{3}m$ phase by Hippler *et al.* [11], it is only recently that thorough characterizations have been reported [17,18]. Moreover, recent theoretical studies on a similar class of materials such as halide perovskites imply *the necessity of including lattice anharmonicity*, in particular, for the reliable prediction of the phase-transition temperature, which matches well with available experimental data. For example, Tadano and Saidi have calculated the cubic-to-tetragonal phase-transition temperature of α-$CsPbBr_3$ (404–423 K) by obtaining a very small difference from the experimental measurement (403 K) [19]. For this outcome, they have included the loop diagram, which consists of quartic interatomic force constants (IFCs), and the contribution of the bubble self-energy term, which consists of cubic IFCs on top of the self-consistent solution. Moreover, Tadano and Tsuneyuki have found that lattice anharmonicity plays an important role in describing the lattice thermal conductivity of type-I clathrate $Ba_8Ga_{16}Ge_{30}$ [20].

In many perovskite materials, the high-symmetry cubic phase is stable at a high temperature, and with decreasing temperature, structures with lower symmetry, such as tetragonal, orthorhombic, and monoclinic phases, become stable. Therefore, in the harmonic phonon band structures of cubic $SrTiO_3$, $BaTiO_3$, and $PbTiO_3$, imaginary frequencies are found [14–16]. Both halide and oxide perovskites are well-known materials and an increasing amount of research is reporting their intriguing characteristics. Antiperovskites are structurally similar to perovskites. However, the atomic positions occupied by cations in perovskites are replaced with anions in antiperovskites and vice versa. In terms of applications, antiperovskite alkali-metal oxyhalides are good candidates for solid-state electrolytes [21]. Cubic Na_3OCl has imaginary frequencies in the M and R modes and 14 possible tilted systems are generated by combining $M_3^+ \oplus R_4^+$ distortions that have lower static energy than the cubic phase [17]. In this paper, the stability of these 14 tilted phases, as well as the cubic phase, are discussed in terms of the Gibbs free energy using the quasiharmonic approximation (QHA) method, which considers the effect of volume expansion to figure out the most stable phase and phase transition during the cooling-down process.

To end this introduction, it is worth emphasizing that previous results for face-centered-cubic metals such as silver and covalent materials such as diamond, graphite, and even the ionic materials such as lighter alkali hydrides (LiH, NaH) have shown the effectiveness of phonon calculations for obtaining P-T phase diagrams and thermodynamic properties using the QHA [22–25]. Notwithstanding, another study on other metals such as Fe, Ni, Ti, and W has shown that the thermodynamic quantities calculated with quasiharmonic phonon calculations are particularly lacking with regard to describing the temperature dependence [26]. Moreover, many studies on the perovskite and antiperovskite materials have shown that careful consideration of lattice anharmonicity is essential for the reliable prediction of the thermodynamic quantities as well as the thermal conductivity and dielectric properties [14,27–30].

This paper is organized into the following sections. Our methodologies are fully detailed in Sec. II, where we describe not only the harmonic and anharmonic approximations (treated within self-consistent phonon theory) but also the atomic scale tools based on density-functional theory. The results are presented in Sec. III. Some conclusions are drawn in Sec. IV.

II. METHODOLOGY OF CALCULATIONS

The harmonic approximation assumes that the second derivative of the potential energy with respect to the atomic displacement is constant. This is a reasonably good approximation, particularly for materials where the atoms are tightly bound through a strong covalent bond. In other words, the shape of the potential-energy surface around the energy minimum is close to a parabolic shape for these materials. However, for materials formed with a relatively weak bond between the constituent atoms, the curvature around the energy minimum easily deviates from a parabolic shape even with a displacement caused by thermal excitation energy equivalent to room temperature. In this case, the anharmonic shape of the potential-energy surface can be interpreted as the change of the effective harmonic frequency depending on the temperature.

For a certain class of materials, the harmonic approximation could be a cost-efficient and reliable way to model material properties. Moreover, there are well-established methods for calculating thermodynamic quantities out of phonon band-structure calculations. However, for some materials that have strong lattice anharmonicity, higher-order force constants need to be considered for the reliable prediction of material properties. Herein, we first draw the P-T phase diagram of Na_3OCl through the Gibbs free energy calculated using the QHA. These calculations enable us to investigate phase change over a wide temperature and pressure range with a relatively small computational cost. Then, we move on to the anharmonic phonon calculations to examine the effect of lattice anharmonicity in the phase transition of the material. Since the number of interatomic force constants increases dramatically if the materials have low symmetry, we select only the high-symmetry cubic phase for this purpose [31,32].

By expanding the harmonic phonon model of lattice dynamics, the QHA describes the thermal expansion of the material. In this approximation, phonon frequencies become volume dependent while the harmonic approximation holds for each volume [33,34]. The QHA turns out to be a good approximation at temperatures far below the melting points [35,36] and many studies have been performed with the QHA to predict the phase-dependent thermodynamic and elastic properties of the materials, which are consistent with experimental reports [15,22–24, 37–43].

The Gibbs free energy $G(T,P)$ is an useful thermodynamic potential in the study of processes at constant temperature T and pressure P. Through examining the free energies $G(T,P)$ of possible crystal phases, phase changes can be monitored by varying two thermodynamic parameters. In our calculations, the Gibbs free energy G is obtained by minimizing the availability of the nonequilibrium Gibbs free energy (G^*) with respect to the volume V at a given T and P, as follows [44]:

$$G(T,P) = \min_V \left[U_{\rm el}(V) + F_{\rm vib}(T,V) + PV\right], \qquad (1)$$

where $U_{\rm el}$ is the total electronic energy, $G^*(T,V,P) \equiv U_{\rm el}(V) + F_{\rm vib}(T,V) + PV$, and $F_{\rm vib}$ is the vibrational free energy. The vibrational free energy can be calculated from the QHA or anharmonic approaches using the phonon density of states. Based on the QHA, the vibrational free energy $F_{\rm vib}$ is expressed as [31]

$$\begin{aligned} F_{\rm vib}(T,V) &= \frac{1}{2}\sum_{qj} \hbar\omega_{qj}(V) \\ &\quad + k_B T \sum_{qj} \ln\left[1 - \exp\left(-\frac{\hbar\omega_{qj}(V)}{k_B T}\right)\right], \qquad (2) \end{aligned}$$

where the index j labels the phonon modes for each crystal momentum vector q.

In the phonon calculations considering lattice anharmonicity, the most important procedure is to determine the IFCs. To this end, it is necessary to have structures with atoms that are displaced from their zero-force positions. If a small number of atoms are displaced, we need to have relatively large structures. Sometimes, it is necessary to have several thousands of structures even for the high-symmetry cubic phase. In this case, the error for the determination of IFCs is very small, since the amount of displacement is constant and the directions of the displacements are along each of three orthogonal axes. Therefore, one important aspect of our methodology is the use of atomic scale calculations to evaluate forces acting on individual atoms that are displaced from their zero-force structure. These effects play a crucial role in determining the impact of anharmonic effects. For this purpose, a first strategy consists of resorting to density-functional theory [45] (DFT) as implemented in the Vienna *ab initio* simulation package (VASP) [46]. The Perdew-Burke-Ernzerhof (PBE) version of the generalized gradient approximation (GGA) [47] is adopted for the exchange-correlation functional. The electron-ion interactions are described by the projector-augmented-wave (PAW) method [48]. The geometries are relaxed using the conjugate-gradient (CG) method until the Hellman-Feynman forces on the individual atoms become less than 0.001 eV/Å. The convergence criterion of the total energy in the self-consistent field (SCF) loop is 10^{-8} eV, with an energy cutoff of 500 eV. The tetrahedron method with Blöchl corrections is chosen for accurate integration over the Brillouin zone.

As a second strategy of structural sampling, we resort to a scheme that is fully rooted into *ab initio* molecular dynamics (AIMD) [49–51]. We initially conduct AIMD simulation, within a Born-Oppenheimer scheme [52], in the canonical *NVT* ensemble by setting the temperature to 300 K. The Nosé-Hoover thermostat is employed [53]. This canonical simulation last for 4 ps, with a time step of 2 fs. From the trajectory obtained, we sample 80 atomic configurations at constant time intervals. Subsequently, in these configurations, all the atoms inside the simulation cell are randomly displaced by 0.1 Å. The atomic forces for the configurations prepared in this manner are obtained using DFT calculations, with an energy cutoff of 500 eV and $4 \times 4 \times 4$ k grids. The methods for structure sampling employed in this study are very much consistent with each other. However, AIMD proves more efficient and it is mostly adopted throughout this study.

When performing SCP calculations (as implemented in the ALAMODE software package [54]), one has to keep in mind that considering lattice anharmonicity is analogous to the quasiparticle (QP) *GW* method in the electronic structure calculations. As the *GW* calculations consider many-body interactions starting from Kohn-Sham eigenstates, the SCP theory considers lattice anharmonicity by solving the Dyson equation, which considers phonon many-body interactions. In doing so, we need to consider three main anharmonic self-energy terms, the so-called tadpole, loop, and bubble diagrams. Each of the three terms can be calculated with the cubic or quartic IFCs (Φ_3, Φ_4). However, finding a fully self-consistent solution of the Green function $G(\omega)$ in the Dyson equation including those three self-energy terms is very challenging because of the bubble self-energy term, which contains an ω dependence. Therefore, the strategy of Tadano *et al.* is initially to obtain a self-consistent solution without the bubble term (SC1).

Then, the fully dressed Green function can be solved with the Dyson equation, which contains frequency-dependent bubble self-energy, and the solution of SC1 as an input phonon propagator. Therefore, the Dyson equation that needs to be solved can be written as follows:

$$\left\{G_q(\omega)\right\}^{-1} \approx \left\{G_q^S(\omega)\right\}^{-1} - \Sigma_q^B\left[G^S, \Phi_3\right](\omega). \quad (3)$$

Tadano *et al.* end up with the following self-consistent equation to deal practically with the above equation [19]:

$$\Omega_{qj}^2 = \left(\omega_{qj}^S\right)^2 - 2\omega_{qj}^S \operatorname{Re}\Sigma_{qj}^B\left[G^S, \Phi_3\right]\left(\omega = \Omega_{qj}\right), \quad (4)$$

where ω_{qj}^S is the self-consistent solution obtained by SC1. Instead of solving the QP frequency for full self-consistent solutions of Eq. (4), which is called quasiparticle-nonlinear (QP-NL), we can obtain a solution similar to the G_0W_0 calculations in the electron many-body calculations. Depending on the ways in which the frequency in the bubble self-energy is approximated in Eq. (4), there are two more levels of approximations [19]. Those correspond to the cases when $\omega = 0$ and $\omega = \omega_{qj}^S$, which are denoted as QP[0] and QP[S], respectively.

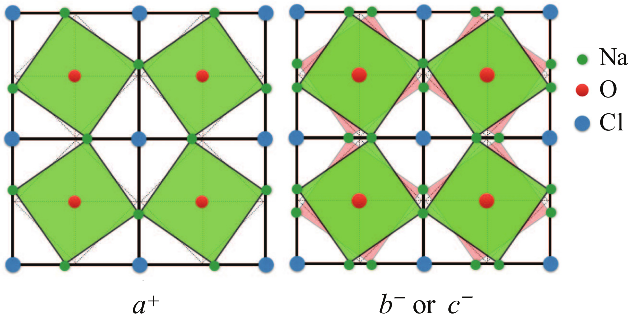

FIG. 1. According to Glazer's notation, the $P2_1/m$ structure also can be represented as $a^+b^-c^-$. Here, a^+ means there is only in-phase rotation of ONa$_6$ octahedra along the [100] direction, which is derived from atomic displacements by the M vibrational soft mode, while b^-c^- means the out-of-phase rotation pattern repeats along the [010] and [001] directions, induced from displacements by the R vibrational soft mode. The dotted squares are drawn to guide the ONa$_6$ octahedra in the cubic phase and the green (in front) and red (behind) squares indicate the tilted octahedra in the $P2_1/m$ phase.

III. RESULTS

A. Quasiharmonic approximation results

We first perform the structural optimization of various polymorphs. The optimized lattice parameter (a_0) of primitive cubic Na$_3$OCl is 4.538 Å. To prepare the structures with octahedral tilting, a $2 \times 2 \times 2$ supercell is used. As we have confirmed in our previous work, the monoclinic structure with $P2_1/m$ symmetry is the most stable in terms of static energy. If we assume the process of octahedral tilting from the $2 \times 2 \times 2$ cubic supercell, this structure can be represented using the Glazer notation as $a^+b^-c^-$, as shown in Fig. 1. This indicates that the structure can be represented as the combination of octahedral tilting along each axis. Here, $a^+b^-c^-$ denotes the in-phase rotation of octahedra along the [100] direction and the out-of-phase rotation of octahedra along the [010] and [001] directions, as illustrated in Fig. 1. We obtain $a = 9.0645$ Å, $b = 9.0625$ Å, and $c = 9.0613$ Å, and $\alpha = 90.01°$, $\beta = 90.00°$, and $\gamma = 90.00°$ for the monoclinic $P2_1/m$ phase in a $2 \times 2 \times 2$ supercell consisting of 40 atoms. Compared to the lattice constant of the cubic phase, there is a 0.13–0.16% decrease in length along each direction. The phonon dispersions of cubic $Pm\bar{3}m$ and 14 tilted structures are generated using a finite displacement method (see Fig. S1 in the Supplemental Material [55]) [56–58], as implemented in the PHONOPY code [31]. The QHA is used to calculate the thermodynamic quantities and estimate the phase transition. For all of the 15 phases, $2 \times 2 \times 2$ supercells with a $4 \times 4 \times 4$ k mesh are used to ensure consistency. We also confirm that the convergence of the cubic phase Gibbs free energy can be achieved with a $4 \times 4 \times 4$ k mesh, as shown in Table S1 of the Supplemental Material [55].

The QHA results in Fig. 2 show the sequence of phase changes from cubic $Pm\bar{3}m$ to orthorhombic $Bmmb$ (denoted by $a^0b^+c^-$) and then to monoclinic $P2_1/m$ (denoted by $a^+b^-c^-$). The cubic phase is the most stable phase at high temperature and low pressure and it has a phase transition to the orthorhombic phase at around 650 K. The orthorhombic $Bmmb$ phase is a tilted phase that results from the condensation of imaginary M and R soft modes. The condensation of the soft mode at M causes in-phase rotation along the y axis and the soft-mode condensation at R induces out-of-phase rotation along the z

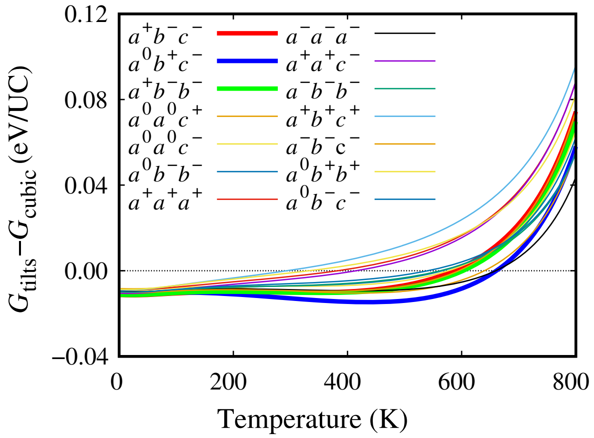

FIG. 2. The temperature-dependent Gibbs free energies (G_{tilts}) at pressure $P = 0$ for 14 tilted structures of Na$_3$OCl relative to the Gibbs free energy for cubic (G_{cubic}) Na$_3$OCl.

axis. With decreasing temperature, the next phase transition is to the monoclinic $P2_1/m$ phase, which is derived from a condensed X soft mode of the $a^0b^+c^-$ phase [59]. This phase transition to the $P2_1/m$ structure is also known to be induced by the combination of M and R soft-phonon condensation from the cubic phase. According to the quasiharmonic phonon calculations, this phase transition is predicted to occur at around 135 K.

To check the convergence of the harmonic force constants with respect to the supercell size, we calculate the root-mean-square (rms) of the difference of the force constants. When the rms is calculated with the force constants of 4 × 4 × 4 supercell as the reference, we find that the rms values of the 1 × 1 × 1, 2 × 2 × 2, and 3 × 3 × 3 supercells are 0.4393, 0.0242, and, 0.0056, respectively. Moreover, we also check the convergence of the free energy in different cell sizes. The results show that the free-energy differences of the cubic phase between the 2 × 2 × 2 supercell and the 3 × 3 × 3, 4 × 4 × 4, and 6 × 6 × 6 supercells are greater than 10^{-2} eV per unit cell (UC). These energy differences are larger than the free-energy differences between the cubic and titled phases and, in turn, this results in a large error in the phase-transition temperature. However, we confirm that in the case of the 4 × 4 × 4 supercell, the free energy converges within 10^{-3} eV/UC. Therefore, the 4 × 4 × 4 supercell (320 atoms) with the 2 × 2 × 2 k mesh is used to ensure consistency. Figures 3(a)–3(d) show the nonequilibrium Gibbs free energies of four phases of Na_3OCl. From the minimum at each temperature curve, the Gibbs free energy G is determined. The difference in the Gibbs free energies between the tilted phase and the cubic phase is illustrated in Fig. 3(e) and it shows that the cubic phase is stabilized at temperatures higher than 220 K. The orthorhombic $Bmmb$ phase is stabilized in the range between 135 K and 220 K. The convergence of the cubic-to-orthorhombic phase-transition temperature with respect to the supercell size is shown in Fig. S2 of the Supplemental Material [55].

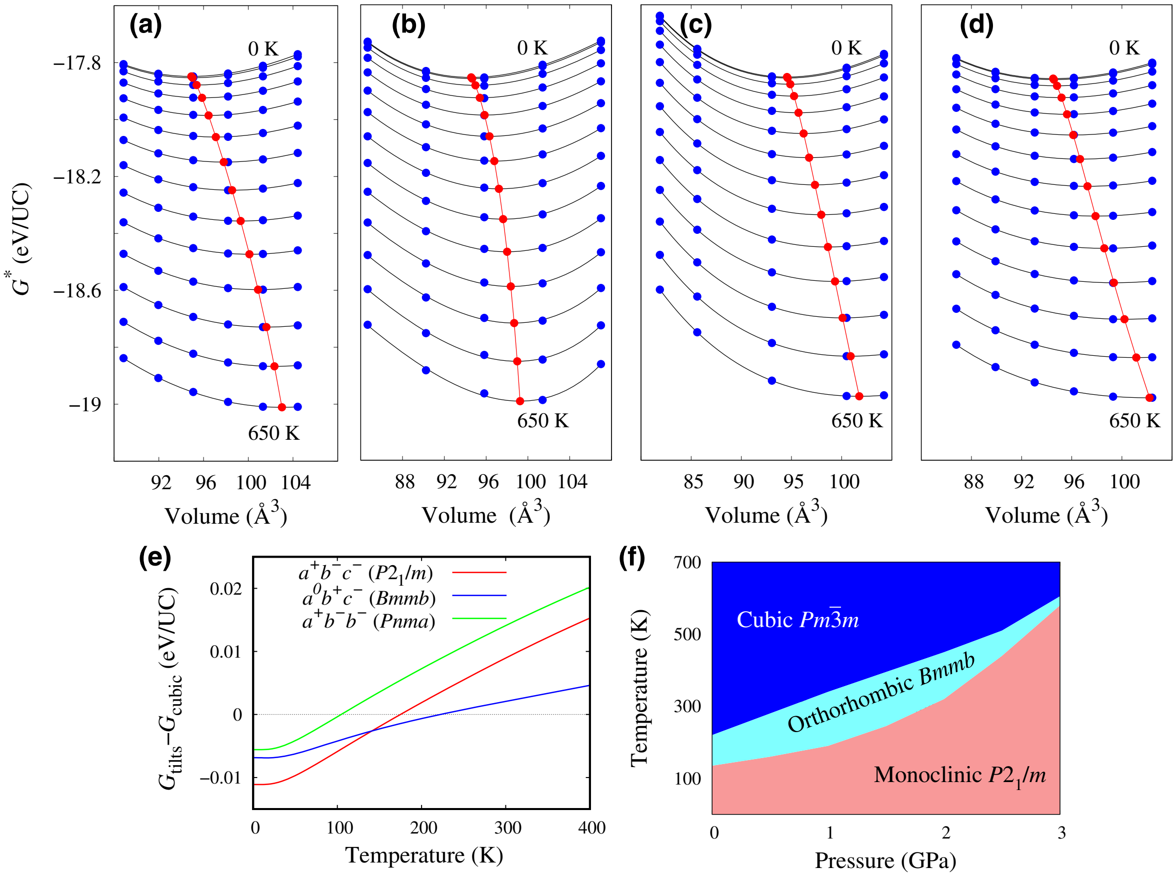

FIG. 3. (a)–(d) The nonequilibrium Gibbs free energies G^* (T, V, P) for the (a) cubic $Pm\bar{3}m$, (b) orthorhombic $Bmmb$, (c) monoclinic $P2_1/m$, and (d) orthorhombic $Pnma$ phases with respect to the volume at zero pressure and different temperatures between 0 K and 650 K are presented by blue circles, with black curves fitted to the Birch-Murnaghan equation of states. From the minima of the respective black curves, the Gibbs free energies at zero pressure are obtained and they are shown with red circles and connected with red lines. (e) The Gibbs-free-energy difference of the orthorhombic $Bmmb$, orthorhombic $Pnma$, and monoclinic $P2_1/m$ phases are comparable to the cubic phase. (f) The P-T phase diagram of Na_3OCl.

This phase-transition result is consistent with the experimental observation stating that the cubic structure is the most stable phase at room temperature and ambient pressure [11]. The phase diagram can be generated by calculating Gibbs free energies as a function of the temperature for the given six different pressures, which are obtained via Eq. (1). Figure 3(f) shows that the room-temperature stable phase is the lower-symmetry phase when the pressure is higher than 0.7 GPa. We propose that Na_3OCl is in the monoclinic $P2_1/m$ phase at a pressure over 2.1 GPa and room-temperature conditions. The orthorhombic phase is observed in the range of pressure between 0.7 and 2.1 GPa and the cubic phase is considered to be the most stable at pressures below 0.7 GPa.

B. Self-consistent phonon calculations

Due to the relatively small computational cost of phonon calculations with the QHA, we are able to examine three different polymorphs and plot the phase diagram with respect to temperature and pressure. Despite this advantage, it is also well known that the QHA has a limitation in the description of lattice anharmonicity. Therefore, we additionally perform self-consistent phonon (SCP) calculations using ALAMODE [54]. These calculations consider not only the second-order but also the fourth-order IFCs at the same time, which enables the description of the phonon frequency change with respect to the temperature [14,60]. We also note that previous calculations on oxide or halide perovskites have already demonstrated that SCP calculations of the high-symmetry cubic phase are useful for prediction of the phase-transition temperature. It is reported in the literature that particular soft phonons lead to phase transition by phonon condensation. Given the structural similarity of Na_3OCl with the perovskite materials, we need to pay attention to the possibility of observing similar behavior [14].

After finishing the force calculations for all sampled structures, we need to determine the IFCs from the raw data. This can be understood as the fitting of IFCs using DFT force data. Therefore, there could be many detailed choices, including regularization methods that are frequently used in machine learning to prevent overfitting. However, we find that simple ordinary-least-squares (OLS) fitting works well here. Sometimes, harmonic force constants are determined first with finite displacement sampling and then the other higher orders of IFCs are determined with the predetermined harmonic FC fixed. This is the preferred method of fitting, since it reduces the possible errors of harmonic FC in the case when all orders of the IFCs are determined simultaneously. Here, we find that the resulting phonon band structures do not change much even when all orders of the IFCs are determined simultaneously. Although IFCs up to quartic terms are used in the SCP calculations, higher orders up to the sixth-order IFCs are also determined for the accuracy of the IFCs that we use [14,60]. All possible combinations of interactions are considered for harmonic and cubic terms and the combinations with distances between atoms of less than 12 bohr, 8 bohr, and 8 bohr are considered for the fourth-, fifth-, and sixth-order IFCs, respectively.

There are imaginary frequencies in the phonon band structures of 12 octahedral tilted structures. However, those imaginary frequencies are neglected in the calculation of the vibrational free energy. Moreover, the strong lattice anharmonicity found in perovskite materials raises the need to apply this method, including the consideration of lattice anharmonicity in the antiperovskite Na_3OCl. For the consideration of lattice anharmonicity, we need to prepare a quartic order of interatomic force constants. However, lower-symmetry structures require a formidable amount of interatomic force constants. Therefore, here we consider only the high-symmetry cubic phase. The phonon band structure of the cubic Na_3OCl phase shows imaginary frequencies at M and R symmetry points. If we consider lattice anharmonicity, these imaginary frequency modes turn into soft-phonon modes with positive frequency. In addition, they tend to have a strong temperature dependence and disappear below a certain temperature. Therefore, through these calculations, we are able to predict the phase-transition temperature. Moreover, the lower-energy structure can be viewed as a small modification of the higher-symmetry structure. Because the modification is caused by the distortion corresponding to the eigenvector of the modes with the imaginary frequency, we can predict the symmetry of the low-temperature phase. With this in mind, we perform SCP calculations as implemented in ALAMODE [54]. In Fig. 4(a), the anharmonic phonon band structures of cubic $Pm\bar{3}m$ Na_3OCl calculated with the SC1 method are shown in the range of temperatures from 200 K to 500 K. We can recognize that by including the fourth-order IFC in the SCP equation, the imaginary phonon frequencies disappear. In doing that, we also find that the q mesh of $8 \times 8 \times 8$ is a reasonable choice in terms of the convergence of soft-mode frequencies at M and R symmetry points (see Table S2 in the Supplemental Material [55]). As shown in Fig. 4(b), the soft-mode frequencies at M and R can be nicely fitted with the equation $\Omega_q^2(T) = a(T - T_C)$. From Fig. 4(b), the result shows that the orthorhombic-to-cubic phase transition occurs at around 86 K, which is an underestimate compared to the QHA result with the $4 \times 4 \times 4$ supercell. It is consistent with the theory that the QHA method neglects the imaginary frequencies while the anharmonic approach takes the effect of these phonon modes into account. As a consequence, the vibrational energy decreases, lowering the free energy of the cubic phase.

The calculated anharmonic phonon dispersion curves using the SC1 approximation are compared to those using the QP method by including the bubble self-energy in

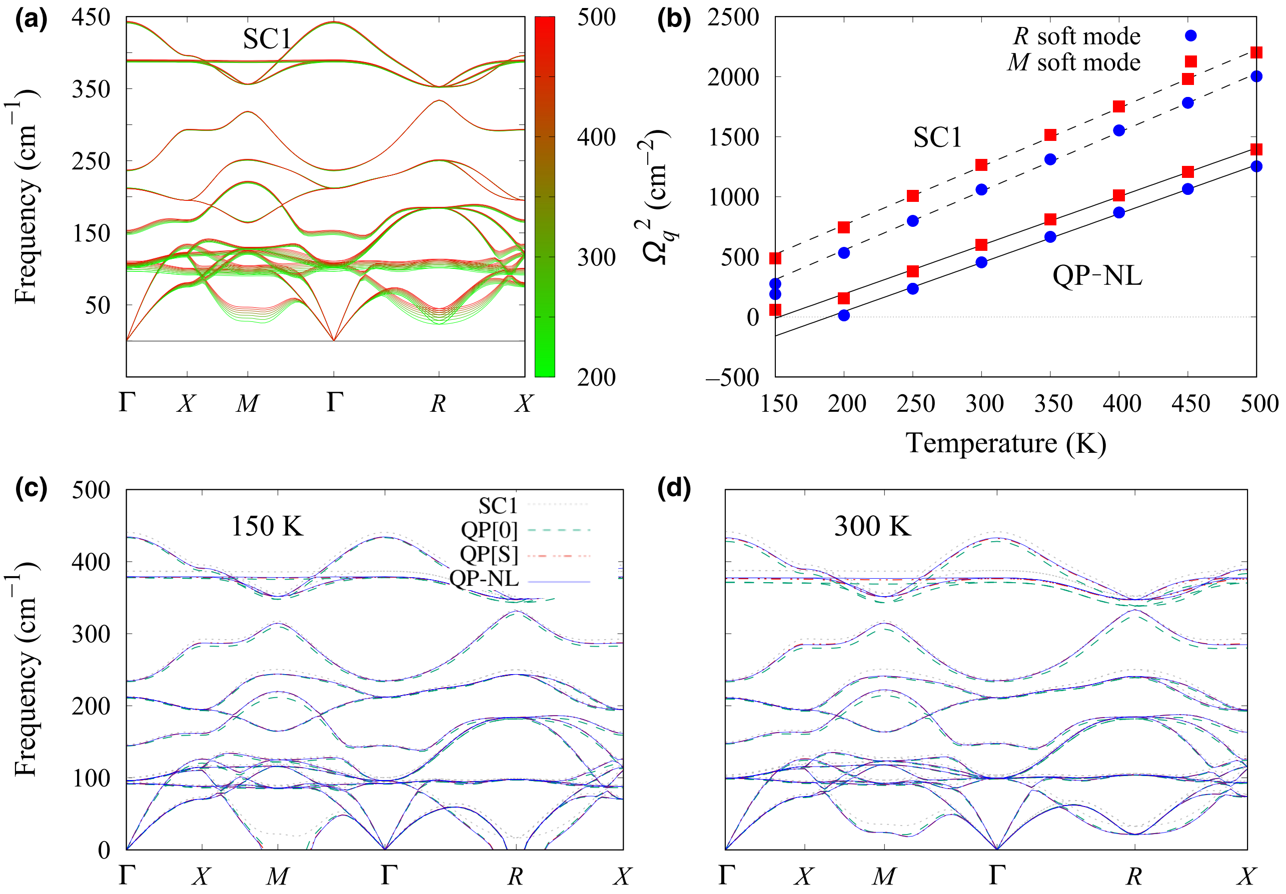

FIG. 4. (a) The phonon band structure at various temperatures from 200 K to 500 K by considering the fourth-order anharmonic contribution. (b) The temperature dependence of the squared phonon frequencies in the M and R modes. (c),(d) Anharmonic phonon dispersion curves of cubic Na_3OCl calculated at 150 K and 300 K (below and above T_C) using different treatments of QP theory. The red dotted lines, green dashed lines, black dash-double-dotted lines, and blue solid lines represent the phonon bands obtained from SC1, QP[0], QP[S], and QP-NL, respectively.

Figs. 4(c) and 4(d). The SC1 phonon frequencies are overestimated compared to the QP frequencies and the overestimation is significant in the soft modes, while the QP[0] and QP[S] results are close to the QP-NL one. The QP[0] frequencies are slightly underestimated in the optical modes, while the QP[S] results are consistent with the QP-NL ones. Similar to the SC1 characteristic, through linear fitting of the temperature dependence of squared phonon frequencies, we can estimate the phase-transition temperature as given in Table I. The QP theory with different treatments gives similar results of about 195 K, which is more than 2 times higher than the transition temperature from the SC1 method, and a similar report is given by Tadano *et al.*. By including the bubble self-energy term on top of the SC1 solution, the authors find that the phase-transition temperatures of halide perovskite become close to the experimental ones [19]. Their estimation of the transition temperature without the bubble term is almost half of the value compared to the experimental one. However, by including the bubble term, they are able to improve the results significantly. Unfortunately, the experimental phase-transition temperatures of Na_3OCl have not been reported yet. Therefore, direct comparison with the experimental data is not available at this point. Nonetheless, the room-temperature stability of the cubic phase reported in the literature suggests that the current computational predictions are at least in a reasonable range.

TABLE I. The cubic-to-orthorhombic phase-transition temperatures are calculated by the QP theory at different levels. The two values in each cell show the transition temperatures estimated from the soft-mode frequency at the M and R points, respectively.

Method	Range of transition temperatures (K)
SC1	54–86
QP[0]	168–195
QP[S]	167–195
QP-NL	166–195

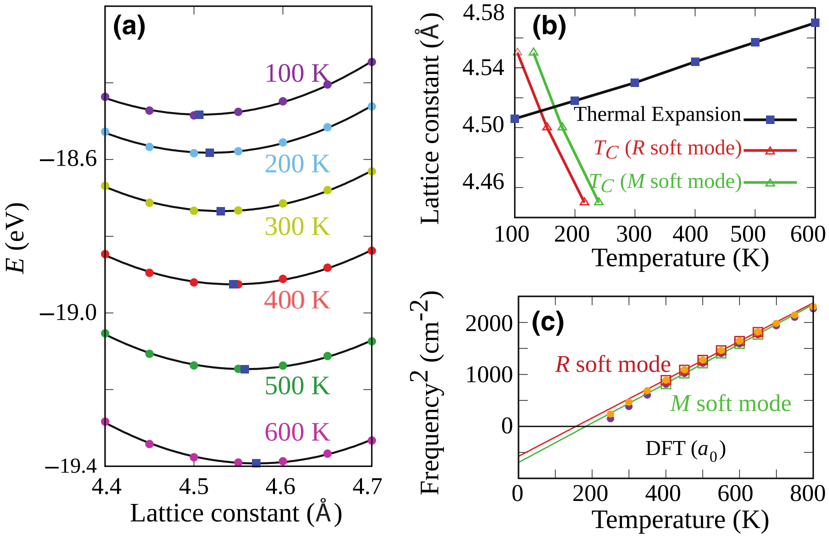

FIG. 5. (a) Helmholtz-free-energy curves at various temperatures from 100 to 600 K. The minimum points at each temperature curve are marked with blue squares. (b) The thermal-expansion line and the lattice constant versus the phase-transition temperature T_C curve. (c) The temperature dependence of the squared phonon frequencies in the M and R modes when the lattice constant is obtained at an energy minimum using the PBEsol functional. The data points marked with empty squares are used for line fitting.

The materials with strong lattice anharmonicity also tend to be sensitive to external strain. Therefore, we need to carefully consider the effect of thermal expansion on the phase-transition temperature. For the reliable prediction of thermal expansion, we adopt the PBEsol exchange-correlation functional. It is demonstrated that the lattice constant calculated with the PBEsol functional [61] is close to the experimental one compared to that estimated with other functionals such as PBE or LDA. Note that without the temperature effect, the lattice constant of the cubic phase is 4.483 Å, which is smaller 1.2% than the PBE lattice constant (4.538 Å). To consider the temperature effect on the lattice constant, the thermal expansion of cubic Na_3OCl is calculated using the Helmholtz-free-energy curves at various temperatures as presented in Fig. 5(a). The minimum points of the energy-lattice constant curves at each temperature are marked with blue squares. As shown in Fig. 5(b), the lattice constant increases almost linearly with increasing temperature. However, we need to keep in mind that the thermal-expansion curve is plotted from calculations with fixed lattice constant. Therefore, it is necessary to have different information that shows the relationship between the lattice constant and T_C. For the estimation of T_C, as shown in Fig. 5(c), a linear relation of square frequencies in the M and R soft modes is used. Note that for the thermal expansion, we use SC1; however, for the estimation of T_C, we use phonon band structures calculated with an additional self-energy term that has a frequency dependence (QP-NL). The data in Fig. 5(c) are the particular case when the lattice constant is obtained at an energy minimum with the PBEsol functional. We can easily recognize that the frequencies at two soft modes are very close, which results in the phase-transition temperature at similar temperatures (152–183 K) due to the condensation of each soft mode. As shown in Fig. 5(b), when the lattice constant increases, the estimated T_C decreases. The crossing point of the thermal-expansion line and the lattice constant versus the T_C curve indicates the phase-transition point after considering thermal expansion. In comparison with T_C in Fig. 5(c), which assumes a fixed lattice constant, the consideration of thermal expansion makes T_C lower by 16–21 K (136 K versus 152 K and 162 K versus 183 K). The effect of thermal expansion seems to be not so significant in this particular material. However, as shown in Fig. 5(b), this can be dependent on how the soft-mode frequency changes when the lattice constant increases.

The electronic structure and ionic transport properties of Na_3OCl are important as the safety and efficiency indicators for electrolyte applications. Since, for safety reasons, an electrolyte is not supposed to conduct electricity, we calculate the electronic band gaps of the 14 tilted phases, including the cubic phase, and find that the band gaps of all the phases fall in the range between 2.01 and 2.03 eV when we use the GGA functional, as shown in Fig. 6. In the previous report by Pham *et al.* [17], the band gaps of the cubic and monoclinic phases increased to around 3.40 eV when the hybrid functional Hyed-Scuseria-Erznerhof (HSE) method was used, while the band gaps were around 2 eV when the GGA functional was used [62]. From these results, we may consider Na_3OCl as an insulator in all the tilted phases. Second, the ionic transport property is obtained by calculating the migration-energy barriers of Na via the vacancy-mediated mechanism [2]

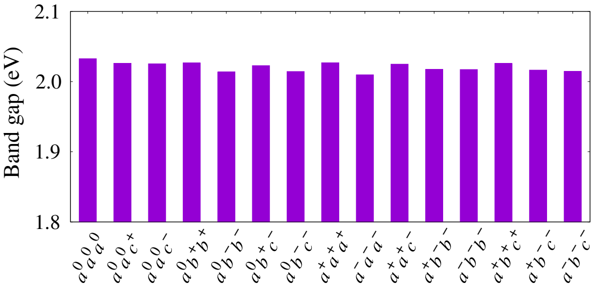

FIG. 6. The band gaps for 15 phases of Na_3OCl.

with the nudged elastic band (NEB) method [63] for the cubic $Pm\bar{3}m$, orthorhombic *Bmmb*, and monoclinic $P2_1/m$ phases. The NEB calculation is performed in a supercell of 40 atoms. The energy-convergence criterion is set to 10^{-3} eV and five intermediate NEB images are used. Figures 7(a)–7(c) show the possible reaction paths of vacancy migration in a schematic way; the $Pm\bar{3}m$ phase has only one path but the *Bmmb* and $P2_1/m$ phases have six and 12 paths, respectively. Figures 7(d)–7(f) show the calculated minimum-energy paths for sodium vacancy migration from one Na site to another in the cubic $Pm\bar{3}m$, orthorhombic *Bmmb*, and monoclinic $P2_1/m$ phases. There are six available migration paths in orthorhombic *Bmmb*, made up of three symmetrically distinct Na sites [64], and 12 paths in $P2_1/m$, composed of four symmetrically distinct Na sites (for the Wyckoff positions in orthorhombic *Bmmb* and monoclinic $P2_1/m$, see Tables S3 and S4 in the Supplemental Material [55]). The single-vacancy migration energies are 0.32–0.35 eV (average 0.34 eV) for monoclinic $P2_1/m$, 0.31–0.35 eV (average 0.34 eV) for orthorhombic *Bmmb*, and 0.30 eV for cubic $Pm\bar{3}m$, respectively. The distorted structures ($P2_1/m$ and *Bmmb* phases) are shown not to have much variation in migration-energy barriers compared to the cubic one. For the cubic phase, the energy barrier (0.30 eV) that we obtain falls between the range of previous reports; the activation energy of Ahiavi *et al.* [65] is 0.29 eV and the migration-energy barrier of Wang *et al.* [66] is 0.43 eV.

IV. CONCLUSIONS

In summary, two types of phonon calculations are performed to investigate the phase transition of antiperovskite Na_3OCl. The first one consists of quasiharmonic phonon calculations. When the Gibbs free energies of 14 different polymorphs are calculated using the QHA, the *P-T* phase diagram shows that three stable phases appear in the limited scopes of temperature and pressure. At ambient pressure, the high-symmetry cubic phase with $Pm\bar{3}m$ symmetry is expected to be stable at temperatures above 205 K and the monoclinic phase with $P2_1/m$ symmetry

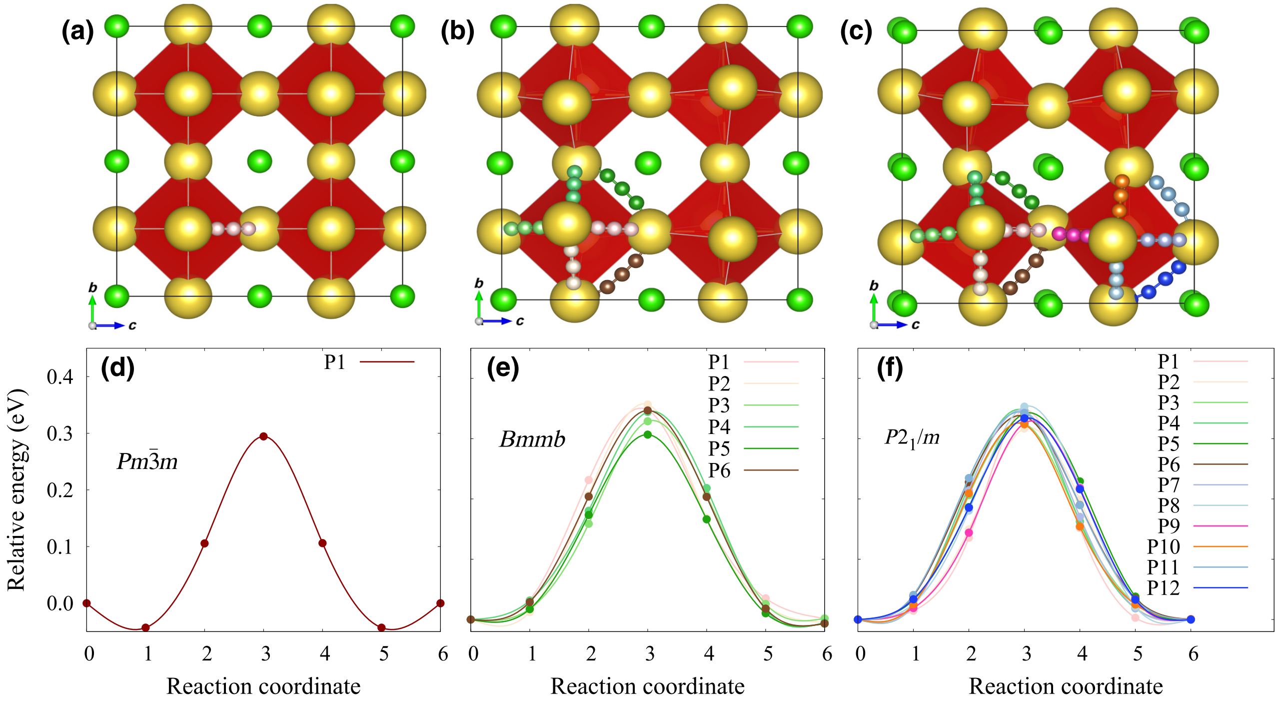

FIG. 7. The reaction paths for Na migration shown using the small colored spheres in the (a) cubic $Pm\bar{3}m$, (b) orthorhombic *Bmmb*, and (c) monoclinic $P2_1/m$ phases and Na, O, and Cl atoms with the larger yellow, red (inside the red octahedra), and green spheres, respectively. The relative energy changes of vacancy migration through the minimum-energy path in the (d) cubic $Pm\bar{3}m$, (e) orthorhombic *Bmmb*, and (f) monoclinic $P2_1/m$ phases, illustrated with various colors for the corresponding reaction paths.

becomes stable below 135 K. In the temperature range between 135 K and 205 K, *Bmmb* is expected to be most stable structure. The second type of phonon calculation involves the inclusion of anharmonic terms by using quartic and cubic IFCs. The phase-transition temperatures (T_C) are calculated using the basic self-consistent phonon calculations (SC1) as well as the temperature-dependent phonon band structures calculated with additional consideration of the bubble self-energy term (QP-NL). Since the latter method corrects the overestimation of the soft-mode frequency, more than twice the phase-transition temperature is expected using the former one (54–86 K versus 166–195 K). The effect of thermal expansion on T_C is not significant in cubic Na_3OCl. Nonetheless, our method shows that the behavior of the soft mode upon lattice constant change could play a critical role in the theoretical determination of the thermal-expansion effects on T_C. The overall results are consistent with the previous computational report on halide perovskite α-$CsPbBr_3$ and the experimentally confirmed room-temperature stability of cubic Na_3OCl. For the three vibrationally stable phases, we calculate the migration-energy barriers of the Na vacancy, and find that the energy barriers falling in the range from 0.30 to 0.34 eV are not much different in their phases.

ACKNOWLEDGMENTS

This work was supported by National Research Foundation of Korea (NRF) grants funded by the Ministry of Science and ICT (MSIT), government of South Korea (Grant No. 2021R1F1A1048555). We wish to thank Dr. Terumasa Tadano, researcher at the National Institute for Material Science (NIMS, Japan), for his helpful comments and discussions.

[1] Y. Zhao and L. L. Daemen, Superionic conductivity in lithium-rich anti-perovskites, J. Am. Chem. Soc. **134**, 15042 (2012).

[2] A. Emly, E. Kioupakis, and A. Van der Ven, Phase stability and transport mechanisms in antiperovskite Li_3OCl and Li_3OBr superionic conductors, Chem. Mater. **25**, 4663 (2013).

[3] K. Chayambuka, G. Mulder, D. L. Danilov, and P. H. L. Notten, From Li-ion batteries toward Na-ion chemistries: Challenges and opportunities, Adv. Energy Mater. **10**, 2001310 (2020).

[4] H. Nguyen, S. Hy, E. Wu, Z. Deng, M. Samiee, T. Yersak, J. Luo, S. P. Ong, and Y. S. Meng, Experimental and computational evaluation of a sodium-rich anti-perovskite for solid state electrolytes, J. Electrochem. Soc. **163**, A2165 (2016).

[5] J.-Y. Hwang, S.-T. Myung, and Y.-K. Sun, Sodium-ion batteries: Present and future, Chem. Soc. Rev. **46**, 3529 (2017).

[6] K. Li, J. Zhang, D. Lin, D.-W. Wang, B. Li, W. Lv, S. Sun, Y.-B. He, F. Kang, Q.-H. Yang, L. Zhou, and T.-Y. Zhang, Evolution of the electrochemical interface in sodium ion batteries with ether electrolytes, Nat. Commun. **10**, 725 (2019).

[7] M. H. Braga, N. S. Grundish, A. J. Murchison, and J. B. Goodenough, Alternative strategy for a safe rechargeable battery, Energy Environ. Sci. **10**, 331 (2017).

[8] M. Wu, B. Xu, X. Lei, K. Huang, and C. Ouyang, Bulk properties and transport mechanisms of a solid state antiperovskite Li-ion conductor Li_3OCl: Insights from first principles calculations, J. Mater. Chem. A **6**, 1150 (2018).

[9] I. Hanghofer, G. J. Redhammer, S. Rohde, I. Hanzu, A. Senyshyn, H. M. R. Wilkening, and D. Rettenwander, Untangling the structure and dynamics of lithium-rich antiperovskites envisaged as solid electrolytes for batteries, Chem. Mater. **30**, 8134 (2018).

[10] R. Chen, W. Qu, X. Guo, L. Li, and F. Wu, The pursuit of solid-state electrolytes for lithium batteries: From comprehensive insight to emerging horizons, Mater. Hor. **3**, 487 (2016).

[11] K. Hippler, S. Sitta, P. Vogt, and H. Sabrowsky, Structure of Na_3OCl, Acta Crystallogr. C. Struct. Commun. **46**, 736 (1990).

[12] M.-H. Chen, A. Emly, and A. Van der Ven, Anharmonicity and phase stability of antiperovskite Li_3OCl, Phys. Rev. B **91**, 214306 (2015).

[13] M. H. Braga, J. A. Ferreira, V. Stockhausen, J. E. Oliveira, and A. El-Azab, Novel Li_3ClO based glasses with superionic properties for lithium batteries, J. Mater. Chem. A **2**, 5470 (2014).

[14] T. Tadano and S. Tsuneyuki, Self-consistent phonon calculations of lattice dynamical properties in cubic $SrTiO_3$ with first-principles anharmonic force constants, Phys. Rev. B **92**, 054301 (2015).

[15] M. C. Oliveira, R. A. P. Ribeiro, E. Longo, M. R. D. Bomio, F. V. Motta, and S. R. de Lazaro, Temperature dependence on phase evolution in the $BaTiO_3$ polytypes studied using ab initio calculations, Int. J. Quantum Chem. **120**, e26054 (2020).

[16] M.-J. Zhou, Y. Wang, Y. Ji, Z.-K. Liu, L.-Q. Chen, and C.-W. Nan, First-principles lattice dynamics and thermodynamic properties of pre-perovskite $PbTiO_3$, Acta Mater. **171**, 146 (2019).

[17] T.-L. Pham, A. Samad, H. J. Kim, and Y.-H. Shin, Computational predictions of stable phase for antiperovskite Na_3OCl via tilting of Na_6O octahedra, J. Appl. Phys. **124**, 164106 (2018).

[18] S. A. Khandy, I. Islam, A. Laref, M. Gogolin, A. K. Hafiz, and A. M. Siddiqui, Electronic structure, thermomechanical and phonon properties of inverse perovskite oxide (Na_3OCl): An ab initio study, Int. J. Energy Res. **44**, 2594 (2020).

[19] T. Tadano and W. A. Saidi, First-Principles Phonon Quasiparticle Theory Applied to a Strongly Anharmonic Halide Perovskite, Phys. Rev. Lett. **129**, 185901 (2022).

[20] T. Tadano and S. Tsuneyuki, Quartic Anharmonicity of Rattlers and Its Effect on Lattice Thermal Conductivity of Clathrates from First Principles, Phys. Rev. Lett. **120**, 105901 (2018).

[21] T. F. J. Dawson and K. Johnston, Anti-perovskites for solid-state batteries: Recent developments, current challenges and future prospects, J. Mater. Chem. **9**, 18746 (2021).

[22] J. Xie, S. de Gironcoli, S. Baroni, and M. Scheffler, First-principles calculation of the thermal properties of silver, Phys. Rev. B **59**, 965 (1999).

[23] N. Mounet and N. Marzari, First-principles determination of the structural, vibrational and thermodynamic properties of diamond, graphite, and derivatives, Phys. Rev. B **71**, 205214 (2005).

[24] W. Yu, C. Jin, and A. Kohlmeyer, First principles calculation of phonon dispersion, thermodynamic properties and B1-to-B2 phase transition of lighter alkali hydrides, J. Phys. Condens. Matter **19**, 086209 (2007).

[25] Z.-G. Mei, S.-L. Shang, Y. Wang, and Z.-K. Liu, Density-functional study of the thermodynamic properties and the pressure-temperature phase diagram of Ti, Phys. Rev. B **80**, 104116 (2009).

[26] P. A. Korzhavyi and J. Zhang, Free energy of metals from quasi-harmonic models of thermal disorder, Metals **11**, 195 (2021).

[27] W. I. Choi, D. J. Yang, D. W. Jung, W.-J. Son, M. Shim, I. Jang, and D. S. Kim, Ab-initio prediction of temperature-dependent dielectric constants and curie temperatures of cubic phase perovskite materials, MRS Commun. **11**, 436 (2021).

[28] W. I. Choi, J. S. An, I. Jang, and D. S. Kim, Strain and temperature-dependent dielectric permittivity of cubic $SrTiO_3$: Self-consistent phonon theory calculations, Curr. Appl. Phys. **29**, 78 (2021).

[29] Y. Zhao, C. Lian, S. Zeng, Z. Dai, S. Meng, and J. Ni, Anomalous electronic and thermoelectric transport properties in cubic Rb_3AuO antiperovskite, Phys. Rev. B **102**, 094314 (2020).

[30] Y. Zhao, C. Lian, S. Zeng, Z. Dai, S. Meng, and J. Ni, Quartic anharmonicity and anomalous thermal conductivity in cubic antiperovskites A_3BO ($A =$ K, Rb; $B =$ Br, Au), Phys. Rev. B **101**, 184303 (2020).

[31] A. Togo and I. Tanaka, First principles phonon calculations in materials science, Scr. Mater. **108**, 1 (2015).

[32] D. C. Wallace, *Thermodynamics of Crystals* (Dover Publications, Mineola, New York, 1998).

[33] A. Otero-de-la-Roza, D. Abbasi-Piérez, and V. Luaña, GIBBS2: A new version of the quasiharmonic model code. II. Models for solid-state thermodynamics, features and implementation, Comput. Phys. Commun. **182**, 2232 (2011).

[34] A. Togo, L. Chaput, I. Tanaka, and G. Hug, First-principles phonon calculations of thermal expansion in Ti_3SiC_2, Ti_3AlC_2, and Ti_3GeC_2, Phys. Rev. B **81**, 174301 (2010).

[35] M. Blanco, E. Francisco, and V. Luaña, GIBBS: Isothermal-isobaric thermodynamics of solids from energy curves using a quasi-harmonic Debye model, Comput. Phys. Commun. **158**, 57 (2004).

[36] Y. Oba, T. Tadano, R. Akashi, and S. Tsuneyuki, First-principles study of phonon anharmonicity and negative thermal expansion in ScF_3, Phys. Rev. Mater. **3**, 033601 (2019).

[37] T. D. Huan, V. Sharma, G. A. Rossetti, and R. Ramprasad, Pathways towards ferroelectricity in hafnia, Phys. Rev. B **90**, 064111 (2014).

[38] B.-T. Wang, P. Zhang, R. Lizárraga, I. Di Marco, and O. Eriksson, Phonon spectrum, thermodynamic properties, and pressure-temperature phase diagram of uranium dioxide, Phys. Rev. B **88**, 104107 (2013).

[39] Z. Deng, Z. Wang, I.-H. Chu, J. Luo, and S. P. Ong, Elastic properties of alkali superionic conductor electrolytes from first principles calculations, J. Electrochem. Soc. **163**, A67 (2016).

[40] S. G. Jabarov, D. P. Kozlenko, S. E. Kichanov, A. V. Belushkin, A. I. Mammadov, B. N. Savenko, R. Z. Mekhtieva, and C. Lathe, Structural studies of the P-T phase diagram of sodium niobate, J. Surf. Invest. X-Ray **6**, 546 (2012).

[41] M. Ahtee, A. M. Glazer, and H. D. Megaw, The structures of sodium niobate between 480 °C and 575 °C, and their relevance to soft-phonon modes, Philos. Mag. **26**, 995 (1972).

[42] A. M. Glazer and H. D. Megaw, The structure of sodium niobate (T2) at 600 °C, and the cubic-tetragonal transition in relation to soft-phonon modes, Philos. Mag. **25**, 1119 (1972).

[43] R. Lizárraga, F. Pan, L. Bergqvist, E. Holmström, Z. Gercsi, and L. Vitos, First principles theory of the hcp-fcc phase transition in cobalt, Sci. Rep. **7**, 3778 (2017).

[44] A. A. Maradudin, G. H. Weiss, and E. W. Montroll, *Theory of Lattice Dynamics in the Harmonic Approximation* (Academic Press, New York, 1963).

[45] W. Kohn and L. J. Sham, Self-consistent equations including exchange and correlation effects, Phys. Rev. **140**, A1133 (1965).

[46] G. Kresse and J. Furthmüller, Efficiency of ab-initio total energy calculations for metals and semiconductors using a plane-wave basis set, Comput. Mater. Sci. **6**, 15 (1996).

[47] J. P. Perdew, K. Burke, and M. Ernzerhof, Generalized Gradient Approximation Made Simple, Phys. Rev. Lett. **77**, 3865 (1996).

[48] G. Kresse and D. Joubert, From ultrasoft pseudopotentials to the projector augmented-wave method, Phys. Rev. B **59**, 1758 (1999).

[49] R. Car and M. Parrinello, Unified Approach for Molecular Dynamics and Density-Functional Theory, Phys. Rev. Lett. **55**, 2471 (1985).

[50] C. Massobrio, A. Bouzid, M. Boero, G. Ori, É. Martin, and S. L. Roux, Chalcogenide glasses for innovation in applied science: Fundamental issues and new insights, J. Phys. D Appl. Phys. **53**, 033002 (2019).

[51] G. Ori, A. Bouzid, É. Martin, C. Massobrio, S. Le Roux, and M. Boero, Chalcogenide glasses as a playground for the application of first-principles molecular dynamics to disordered materials, Solid State Sci. **95**, 105925 (2019).

[52] M. Born and O. R., Zur Quantentheorie der Molekeln, Ann. Phys. **IV. Folge**, 457 (1927).

[53] W. G. Hoover, Canonical dynamics: Equilibrium phase-space distributions, Phys. Rev. A **31**, 1695 (1985).

[54] N. R. Werthamer, Self-consistent phonon formulation of anharmonic lattice dynamics, Phys. Rev. B **1**, 572 (1970).

[55] See the Supplemental Material at http://link.aps.org/supplemental/10.1103/PhysRevApplied.19.034004 for the phonon dispersion of non-tilted and 14-tilted structures of

Na_3OCl, the supercell size and k-mesh convergence check of Gibbs free energy, soft-modes frequencies convergence, and Wyckoff positions of orthorhombic *Bmmb* and monoclinic $P2_1/m$.

[56] D. Alfé, PHON: A program to calculate phonons using the small displacement method, Comput. Phys. Commun. **180**, 2622 (2009).

[57] L. Chaput, A. Togo, I. Tanaka, and G. Hug, Phonon-phonon interactions in transition metals, Phys. Rev. B **84**, 094302 (2011).

[58] K. Esfarjani and H. T. Stokes, Method to extract anharmonic force constants from first principles calculations, Phys. Rev. B **77**, 144112 (2008).

[59] R. B. Sadok, D. Hammouténe, and N. Plugaru, New phase transitions driven by soft phonon modes for $CsPbBr_3$: Density functional theory study, Phys. Status Solidi (B) **258**, 2000289 (2021).

[60] T. Tadano, Y. Gohda, and S. Tsuneyuki, Anharmonic force constants extracted from first-principles molecular dynamics: Applications to heat transfer simulations, J. Phys. Condens. Matter **26**, 225402 (2014).

[61] J. P. Perdew, A. Ruzsinszky, G. I. Csonka, O. A. Vydrov, G. E. Scuseria, L. A. Constantin, X. Zhou, and K. Burke, Restoring the Density-Gradient Expansion for Exchange in Solids and Surfaces, Phys. Rev. Lett. **100**, 136406 (2008).

[62] J. Heyd and G. E. Scuseria, Efficient hybrid density functional calculations in solids: Assessment of the Heyd-Scuseria-Ernzerhof screened Coulomb hybrid functional, J. Chem. Phys. **121**, 1187 (2004).

[63] D. Sheppard, R. Terrell, and G. Henkelman, Optimization methods for finding minimum energy paths, J. Chem. Phys. **128**, 134106 (2008).

[64] S. Fujii, S. Gao, C. Tassel, T. Zhu, T. Broux, K. Okada, Y. Miyahara, A. Kuwabara, and H. Kageyama, Alkali-rich antiperovskite M_3FCh (M = Li, Na; Ch = S, Se, Te): The role of anions in phase stability and ionic transport, J. Am. Chem. Soc. **143**, 10668 (2021).

[65] E. Ahiavi, J. Dawson, U. Kudu, M. Courty, M. S. Islam, O. Clemens, C. Masquelier, and T. Famprikis, Mechanochemical synthesis and ion transport properties of Na_3OX (X = Cl, Br, I and BH_4) antiperovskite solid electrolytes, J. Power Sources **471**, 228489 (2020).

[66] Y. Wang, Q. Wang, Z. Liu, Z. Zhou, S. Li, J. Zhu, R. Zou, Y. Wang, J. Lin, and Y. Zhao, Structural manipulation approaches towards enhanced sodium ionic conductivity in Na-rich antiperovskites, J. Power Sources **293**, 735 (2015).